Available online at www.sciencedirect.com
SCIENCE DIRECT®
International Journal of Heat and Fluid Flow 26 (2005) 613–621
International Journal of HEAT AND FLUID FLOW
www.elsevier.com/locate/ijhff

A study of low-power density laser welding process with evolution of free surface

Eung-Ji Ha [a], Woo-Seung Kim [b,*]

[a] Department of Mechanical Engineering, Hanyang University, 17 Haengdang-dong, Seongdong-gu, Seoul 133-791, South Korea
[b] Department of Mechanical Engineering, Hanyang University, 1271 Sa-1 Dong, Sangnok-gu, Ansan, Kyeonggi-do 425-791, South Korea

Accepted 31 March 2005
Available online 3 June 2005

Abstract

In this study, numerical investigation has been performed on the evolution of weld pool geometry with moving free surface during low-energy density laser welding process. The free surface elevates near the weld pool edge and descends at the center if $d\sigma/dT$ is dominantly negative. It is shown that the predicted width and depth of the weld pool with moving free surface are a little greater than those with flat weld pool surface. It is also believed that the oscillation of the weld pool surface during the melting process augments the rate of convective heat transfer in the weld pool. The present analysis with moving free surface should be considered when Peclet number is greater and Weber number is much smaller than one since the deformation of the weld pool surface is noticeable as *Pe* number increases and *We* number decreases, especially when $\sqrt{Pe}/We$ is greater than the order of 10.

Keywords: Laser welding; Free surface flow; Marangoni convection; Continuum surface force

1. Introduction

Lasers are very efficient means in performing precise industrial welding process, because they have a number of attractive features such as high welding strength, high welding speed, and minimal heat-affected region than TIG(tungsten inert gas) welding, CO_2 welding, and other welding processes. Incident laser beam is partially reflected off the target surface, and the remains are absorbed by the target material, which consequently raises the temperature of the target surface above melting point. According to the power density of the incident laser beam, laser welding process is generally divided into low-power density laser welding and high-power density laser welding (Bauerle, 1996). In low-power density laser welding as shown in the Fig. 1, the weld pool is created by melting the material and the fluid flow in the weld pool is driven dominantly by the spatial variation of the surface tension in the weld pool surface caused by the large temperature gradient. The weld pool created by low-power laser welding has no keyhole formation. The width of the weld pool by low-power laser welding is wider than that by high-power laser welding. The depth of the weld pool generated by low-power laser welding is shallower than the one by high-power laser welding. During laser welding processes, the fluid flow and heat transfer in the weld pool significantly affect the width and depth of the weld pool. Studies have shown that the modeling of the laser welding process is very complex since its modeling includes the phenomena such as thermal conduction/convection in phase-change system and fluid flow with free surface effects. There are many previous works (Duley, 1999; Chan et al., 1984; Basu and Debroy, 1992; Kim and Sim, 1997; Robert and Debroy, 2001) dealing with the shape

* Corresponding author. Tel.: +82 31 400 5248; fax: +82 31 418 0153.
E-mail address: wskim@hanyang.ac.kr (W.-S. Kim).

0142-727X/$ - see front matter © 2005 Elsevier Inc. All rights reserved.
doi:10.1016/j.ijheatfluidflow.2005.03.009

Nomenclature

a	coefficient of solution matrix
c_p	specific heat (J/kg K)
$\mathrm{d}\sigma/\mathrm{d}T$	temperature coefficient of surface tension (N/m K)
δh	grid size (m)
f	volume fraction of material
F_{sa}	surface tension force per unit area (N/m^2)
F_{sv}	surface tension force per unit volume (N/m^3)
g	volume fraction of liquid material
k	thermal conductivity (W/m K)
L	latent heat of fusion (J/kg)
$\vec{n}$	normal vector
p	pressure (Pa)
r	coordinate in radial direction
r_0	radius of laser beam (m)
S	source term
T	temperature (K)
t	time (s)
$\hat{t}$	unit tangential vector
u	velocity (m/s)
$\tilde{u}$	auxiliary velocity computed from incremental changes in u^n (m/s)
z	coordinate in vertical (axial) direction
$[f]$	jump in VOF function

Greeks

α	thermal diffusivity (m^2/s)
κ	curvature of surface (m^{-1})
σ	surface tension (N/m)
μ	dynamic viscosity (kg/m s)

Subscripts

nb	neighboring nodes to node point
p	node point
r	radial direction
s	tangential direction
z	vertical (axial) direction

Superscripts

m	current iteration time level
$m+1$	next iteration time level
n	previous time level
$n+1$	current time level

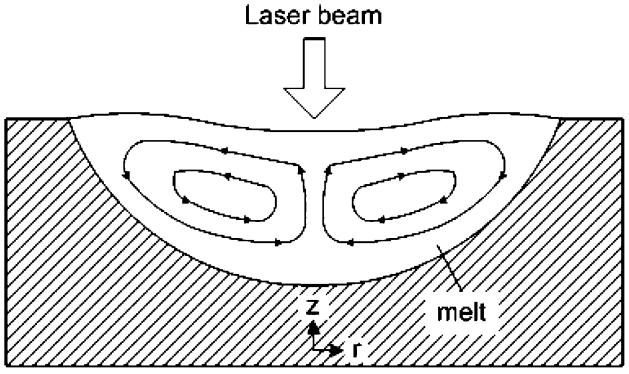

Fig. 1. Schematic representation of the melt pool dynamics in conduction welding.

and size of the weld pool in relation to various laser parameters with non-deformable weld pool surface. Recently, Marathe and Ravi (2004) performed numerical modeling of Marangoni convection with free surface in the Arbitrary Lagrangian Eulerian frame and it was applied laser melting problem. However, the effects of free surface evolution and dimensionless parameters during laser welding have not been extensively examined up to now.

In this study, the free surface evolution is numerically traced by using fixed meshes. The numerical results are validated by comparing the experimental data for laser spot welding on steel (Pitscheneder et al., 1996), gallium (Limmaneevichitr and Kou, 2000) and alumina (Hirsch et al., 1998) plate. The volume-of-fluid (VOF) method (Rider and Kothe, 1998) and modified continuum surface force (CSF) method (Brackbill et al., 1992) are employed in this study to incorporate Marangoni effect with deformable free surface.

2. Numerical model description

2.1. Governing equation

The Eulerian finite difference model considered in this work couples a two-dimensional axisymmetric Navier–Stokes equation solver for fluid flow with free surfaces using RIPPLE (Kothe and Mjolsness, 1991) and energy equation with source-based solidification algorithm (Swaminathan and Voller, 1993). The tracking of free surface is given by the VOF transport equations with piecewise-linear interface calculation (PLIC) method (Rider and Kothe, 1998). The governing equations considered in this study are as follows:

Continuity equation:

$$\frac{1}{r}\frac{\partial}{\partial r}(ru_r)+\frac{\partial}{\partial z}(u_z)=0 \tag{1}$$

Momentum equation:

$$\rho\frac{\partial u_r}{\partial t}+\rho u_r\frac{\partial u_r}{\partial r}+\rho u_z\frac{\partial u_r}{\partial z} = -\frac{\partial p}{\partial r}+\mu\left[\frac{\partial^2 u_r}{\partial r^2}+\frac{\partial^2 u_r}{\partial z^2}+\frac{1}{r}\frac{\partial u_r}{\partial r}-\frac{u_r}{r^2}\right]+S_{u_r} \quad (2)$$

$$\rho\frac{\partial u_z}{\partial t}+\rho u_r\frac{\partial u_z}{\partial r}+\rho u_z\frac{\partial u_z}{\partial z} = -\frac{\partial p}{\partial z}+\mu\left[\frac{\partial^2 u_z}{\partial r^2}+\frac{\partial^2 u_z}{\partial z^2}+\frac{1}{r}\frac{\partial u_z}{\partial r}\right]+S_{u_z} \quad (3)$$

Volume-of-fluid equation:

$$\frac{\partial f}{\partial t}+u_r\frac{\partial f}{\partial r}+u_z\frac{\partial f}{\partial z}=0 \quad (4)$$

Energy equation:

$$\rho c_p\frac{\partial T}{\partial t}+\rho c_p u_r\frac{\partial T}{\partial r}+\rho c_p u_z\frac{\partial T}{\partial z} = \frac{1}{r}\frac{\partial}{\partial r}\left(kr\frac{\partial T}{\partial r}\right)+\frac{\partial}{\partial z}\left(k\frac{\partial T}{\partial z}\right)-\rho L\frac{\partial g}{\partial t}+S_T \quad (5)$$

In Eqs. (2), (3) and (5), S_{u_r} and S_{u_z} are momentum source terms due to the surface tension effect and S_T is an energy source term due to the absorption of incident laser beam. In this work, a two-step projection method (Kothe and Mjolsness, 1991) is introduced to solve the continuity and momentum equation. In the two-step projection method, Eqs. (2) and (3) are approximated as follows:

$$\frac{\tilde{u}_r-u_r^n}{\delta t}=-u_r^n\frac{\partial u_r^n}{\partial r}-u_z^n\frac{\partial u_r^n}{\partial z}-\frac{\mu}{\rho^n}\left[\frac{\partial^2 u_r^n}{\partial r^2}+\frac{\partial^2 u_r^n}{\partial z^2}+\frac{1}{r}\frac{\partial u_r^n}{\partial r}-\frac{u_r^n}{r^2}\right]+\frac{S_{u_r}^n}{\rho^n} \quad (6.1)$$

$$\frac{u_r^{n+1}-\tilde{u}_r}{\delta t}=-\frac{1}{\rho^n}\frac{\partial p^{n+1}}{\partial r} \quad (6.2)$$

$$\frac{\tilde{u}_z-u_z^n}{\delta t}=-u_r^n\frac{\partial u_z^n}{\partial r}-u_z^n\frac{\partial u_z^n}{\partial z}-\frac{\mu}{\rho^n}\left[\frac{\partial^2 u_z^n}{\partial r^2}+\frac{\partial^2 u_z^n}{\partial z^2}+\frac{1}{r}\frac{\partial u_z^n}{\partial r}\right]+\frac{S_{u_z}^n}{\rho^n} \quad (7.1)$$

$$\frac{u_z^{n+1}-\tilde{u}_z}{\delta t}=-\frac{1}{\rho^n}\frac{\partial p^{n+1}}{\partial z} \quad (7.2)$$

Eqs. (1), (6.2) and (7.2) can be combined into a single pressure Poisson equation given below and tilde velocities, $\tilde{u}_r$ and $\tilde{u}_z$, are obtained by the Eqs. (6.1) and (7.1).

$$\frac{1}{r}\frac{\partial}{\partial r}\left(r\frac{1}{\rho^n}\frac{\partial p^{n+1}}{\partial r}\right)+\frac{\partial}{\partial z}\left(\frac{1}{\rho^n}\frac{p^{n+1}}{\partial z}\right) = -\left(\frac{1}{r}\frac{\partial}{\partial r}(r\tilde{u}_r)+\frac{\partial\tilde{u}_z}{\partial z}\right)\Big/\delta t \quad (8)$$

and it can be solved by using an incomplete Cholesky conjugate gradient (ICCG) method. Volume-averaged enthalpy method (Swaminathan and Voller, 1993) is used to solve the energy equation and the velocity in the solid phase is assumed to be zero. Eq. (5), subject to appropriate boundary and initial conditions, can be integrated fully implicitly as

$$a_P T_P^{m+1}=a_P^n T_P^n+\sum_{\mathrm{nb}}a_{\mathrm{nb}}T_{\mathrm{nb}}^{m+1}+\rho L(g_P^n-g_P^{m+1}) \quad (9)$$

where superscript m represents the current iteration level and n represents the previous time level. The above system of equations is non-linear since the liquid fraction depends on temperature. A truncated Taylor series expansion for g^{m+1} gives

$$g^{m+1}=g^m+\frac{\mathrm{d}g}{\mathrm{d}T}\left[T^{m+1}-T^m\right] \quad (10)$$

Substitution of Eq. (10) into Eq. (9) yields a linear source term in the temperature and results in the iterative equation as follows:

$$\left[a_P+\rho L\frac{\mathrm{d}g}{\mathrm{d}T}\right]T_P^{m+1}=a_P^n T_P^n+\rho L\frac{\mathrm{d}g}{\mathrm{d}T}T_P^m+\sum_{\mathrm{nb}}a_{\mathrm{nb}}T_{\mathrm{nb}}^{m+1}+\rho L(g_P^n-g_P^m) \quad (11)$$

At the surface of the weld pool, Marangoni effect is incorporated by relating the shear stress to the spatial gradient of surface tension as follows:

$$-\mu\frac{\mathrm{d}u_r}{\mathrm{d}z}=\frac{\mathrm{d}\sigma}{\mathrm{d}r}=\frac{\mathrm{d}\sigma}{\mathrm{d}T}\frac{\mathrm{d}T}{\mathrm{d}r} \quad (12)$$

$\mathrm{d}\sigma/\mathrm{d}T$ is the temperature coefficient of the surface tension. In general, $\mathrm{d}\sigma/\mathrm{d}T$ is negative for pure material but it can be positive for non-metallic components of compound. It is difficult to directly use the boundary condition given by Eq. (12) at the moving free surface. In this work, the tangential CSF model is introduced in Section 2.2. This model can convert the boundary condition given by Eq. (12) to the volumetric source terms in the momentum equation. Hence, it is convenient to consider Marangoni effect at either the fixed flat surface or the moving free surface using the tangential CSF model.

2.2. Normal and tangential CSF model

The following CSF model interprets the surface tension effect as a continuum body force:

$$\lim_{h\to 0}\int_{\Delta V}\vec{F}_{\mathrm{sv}}(\vec{x}_s)\mathrm{d}^3x=\int_{\Delta A}\vec{F}_{\mathrm{sa}}(\vec{x}_s)\,\mathrm{d}A \quad (13)$$

$\vec{F}_{\mathrm{sa}}$ is the surface tension for the unit surface area. In Eq. (13), the normal surface force for the unit volume is given as (Brackbill et al., 1992)

$$\vec{F}_{\mathrm{sv}}^{(n)}(\vec{x}_s)=\sigma\kappa(\vec{x}_s)\nabla f \quad (14)$$

The tangential surface force for the unit volume can be also written as

$$\vec{F}_{sv}^{(t)}(\vec{x}_s) = \frac{d\sigma}{ds}\hat{t}(\vec{x}_s)|\vec{n}(\vec{x}_s)| \tag{15}$$

where normal vector, $\vec{n}$, is approximated by using the grid size, δh (Brackbill and Kothe, 1996):

$$\vec{n} \cong \frac{[f]}{\delta h}\hat{n} = \frac{\hat{n}}{\delta h} \tag{16}$$

Eq. (15) is rewritten by using Eq. (16) as follows:

$$\vec{F}_{sv}^{(t)}(\vec{x}_s) = \frac{d\sigma}{ds}\hat{t}(\vec{x}_s)\Big/\delta h \tag{17}$$

where (Sasmal and Hochstein, 1994)

$$\frac{d\sigma}{ds}\hat{t} = \left[\hat{i}\left(\hat{t}_r^2\frac{\partial\sigma}{\partial r} + \hat{t}_r\hat{t}_z\frac{\partial\sigma}{\partial z}\right) + \hat{j}\left(\hat{t}_z^2\frac{\partial\sigma}{\partial z} + \hat{t}_r\hat{t}_z\frac{\partial\sigma}{\partial r}\right)\right] \tag{18}$$

Using Eqs. (15) and (17), the volumetric momentum source terms, S_{u_r} and S_{u_z}, that appeared in Eqs. (2) and (3), are given as

$$S_{u_r} = \sigma\kappa n_r + \nabla_s\sigma_r/\delta h \tag{19}$$

$$S_{u_z} = \sigma\kappa n_z + \nabla_s\sigma_z/\delta h \tag{20}$$

2.3. Dimensionless parameters

There are two dimensionless parameters affecting the shape of the weld pool: Peclet (*Pe*) number and Marangoni (*Ma*) number. They are defined as

$$Ma = \frac{-\frac{d\sigma}{dT}\Delta TR}{\mu\alpha} \tag{21}$$

$$Pe = \frac{RV}{\alpha} = \frac{\text{heat by convection}}{\text{heat by conduction}} \tag{22}$$

ΔT is the temperature difference between the edge and center of the weld pool. R and V are the radius of the weld pool and maximum surface velocity, respectively. Weber (*We*) number is the additional dimensionless parameter which determines the magnitude of the weld pool deformation.

$$We = \frac{\rho V^2 R}{\sigma} \tag{23}$$

3. Results and discussions

The present numerical results are compared to the experimental data. The numerical solution with non-deformable weld pool surface is also validated to show that our numerical model can accurately simulate low-power density laser welding process. The results with the tangential CSF model for both the flat surface and the free surface are compared to those for the flat surface with the boundary condition given by Eq. (12). The Prandtl (*Pr*) number for the steel, gallium, and alumina used in the analysis is 0.189, 0.024, and 3.17, respectively.

3.1. Weld pool calculation for the steel

In this case, numerical calculation has been performed for the CO_2 laser welding experiment conducted by Pitscheneder et al. (1996) Laser power distribution is top hat and target is Böhler S 705 Fe–S. The surface tension and the coefficient of surface tension for steel is not a constant but function of temperature and sulfur composition (Sahoo et al., 1988) as shown in Eqs. (24) and (25).

$$\sigma = \sigma_m^0 - A(T - T_m) - RT\Gamma_s \ln\left[1 + k_l a_i e^{-(\Delta H^0/RT)}\right] \tag{24}$$

$$\frac{d\sigma}{dT} = -A - R\Gamma_s \ln(1 + Ka_i) - \frac{Ka_i}{(1 + Ka_i)}\frac{\Gamma_s\Delta H^0}{T} \tag{25}$$

where σ_m^0, A, a_i, Γ_s, ΔH^0, and k_l are the surface tension, temperature coefficient of pure iron, thermodynamic activity of sulfur, standard heat of absorption, and entropy factor, respectively. Equilibrium constant K is given as $k_l e^{-(\Delta H^0/RT)}$. Fig. 2 shows the coefficient of surface tension for 20 ppm and 150 ppm Fe–S with respect to temperature. It is shown in Fig. 2 that $d\sigma/dT$ maintains negative value in the temperature range over 1700 K for 20 ppm Fe–S. The material properties and other information pertaining to the simulation are given in Table 1. The 30×35, 42×50, and 50×60 grid systems are used for grid dependency test and they have non-uniform grid spacing with denser grids in the region adjacent to the weld pool. Fig. 3 shows the weld pool

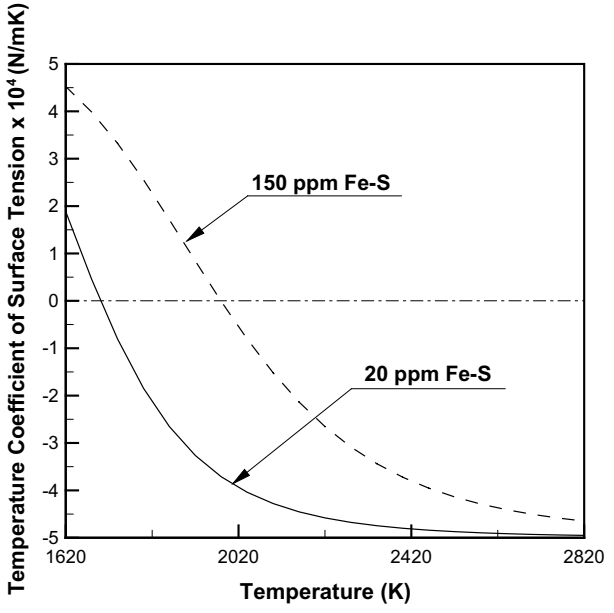

Fig. 2. Temperature coefficient of surface tension for Fe–S as a function of temperature and sulfur activity.

Table 1
Data used for calculation of velocity and temperature fields (Pitscheneder et al., 1996)

Property/parameter	Value
Density (kg/m^3)	8100.0
Melting point (K)	1620.0
Viscosity (kg/m s)	6.0×10^{-3}
Thermal conductivity of solid and liquid (J/m s K)	22.9
Specific heat of solid (J/kg K)	627.0
Specific heat of liquid (J/kg K)	723.14
Latent heat of melting (J/kg)	250.8×10^{3}
Absorption coefficient	3.33×10^{-4}
Beam radius (m)	1.4×10^{-3}
Laser power (W)	5200
Target radius (m)	1.5×10^{-2}
Target thickness (m)	1.5×10^{-2}

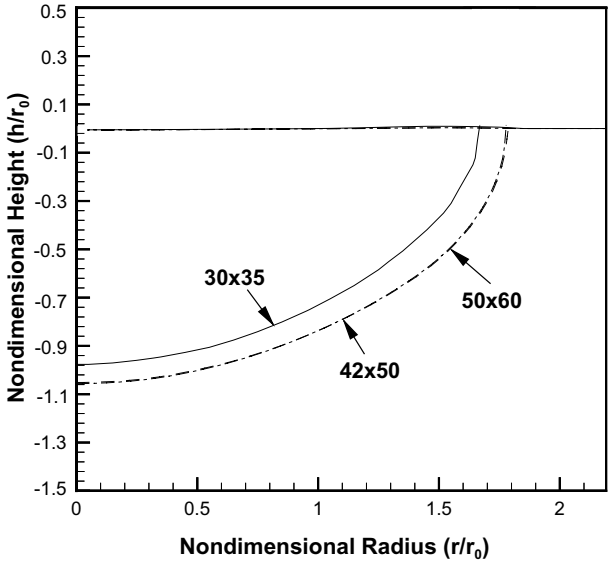

Fig. 3. Grid dependency of weld pool geometry for 20 ppm Fe–S with irradiation time of 5 s.

geometry for 20 ppm Fe–S with irradiation time of 5 s, with respect to grid size. The numerical mass losses of the target material during the calculation of free surface deformation for the 30×35, 42×50, and 50×60 grid systems are very small, and they are -0.0017%, -0.0001%, and -0.0002%, respectively. Fig. 4 indicates the magnified free surface profile of the weld pool for the 20 ppm Fe–S for irradiation time of 5 s with respect to grid size when $d\sigma/dT$ is dominantly negative. It is noted that the free surface profiles converge as the grid systems are denser and the weld pool surface elevates near the edge and descends at the center. Thus, the result from the 42×50 grid system, showing converged weld pool shape and small mass error, is used for the following discussion. Fig. 5 presents the comparison of the predicted weld depth and width to that of the experimental data. The width and depth of the weld pool grow rapidly in the early stage of the welding process and converges to

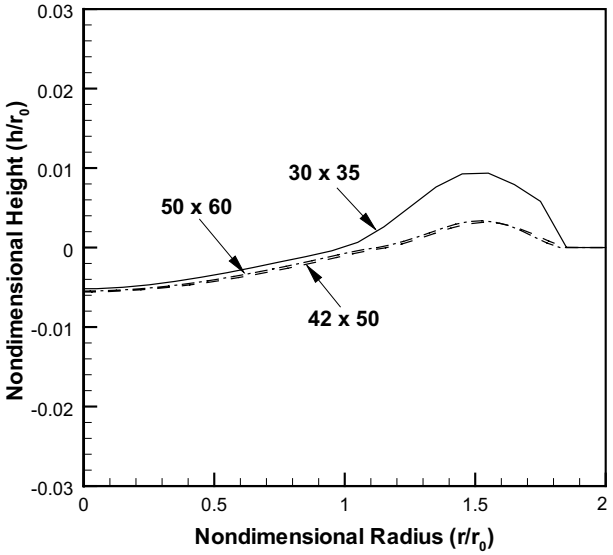

Fig. 4. Free surface profile of weld geometry for 20 ppm Fe–S with irradiation time of 5 s.

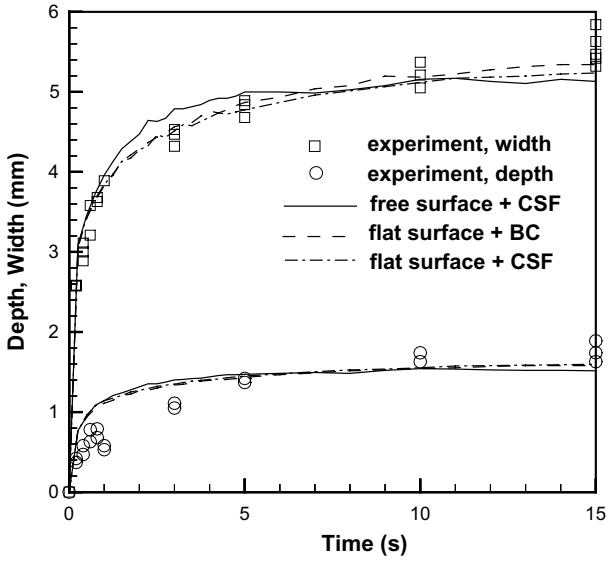

Fig. 5. Comparison of the predicted weld pool depth and width to the experiment (Pitscheneder et al., 1996) for 20 ppm Fe–S with respect to time.

the quasi-steady state as irradiation time passes 5 s. Fig. 6 shows the comparison of the predicted aspect ratio, defined as depth to width of the weld pool, to that of the experimental data. The aspect ratio of the weld pool is almost constant except during the early stage in the welding process. It is shown that the width and depth of the weld pool with deformation is a little larger than that without deformation in transient state, but they are a little smaller than that without deformation in steady state. The oscillation of the weld pool is enhanced with deformation of the weld surface. It is believed that oscillation of the weld pool surface during the early stage of

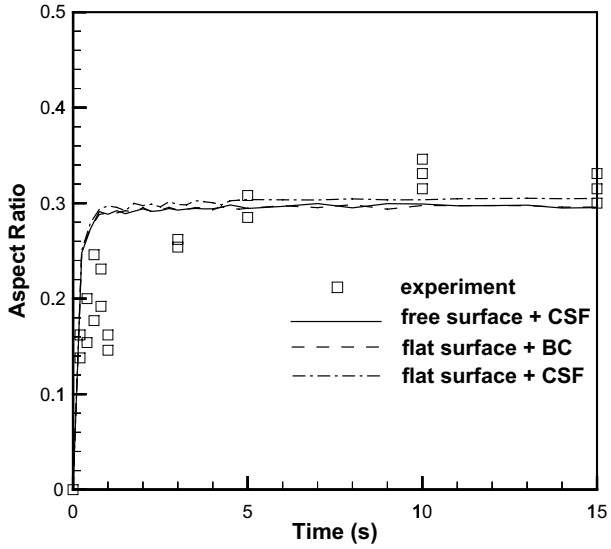

Fig. 6. Comparison of the predicted aspect ratio to the experiment (Pitscheneder et al., 1996) for 20 ppm Fe–S with respect to time.

the melting process augments the convective heat transfer rate in the weld pool. Fig. 7 indicates the comparison of the weld pool size with and without free surface effect. The results show that the shapes of the weld pool are almost identical but the weld pool width and depth with free surface evolution are about 3% greater than those without free surface evolution. The *Pe* number of the steel weld pool is about 172 at 5 s and *We* number is 1.14. Fig. 8 shows the comparison of the predicted weld geometry to that of the experimental data. It is shown that our numerical method reasonably simulates the low-power laser welding process by considering the free surface motion of the weld pool.

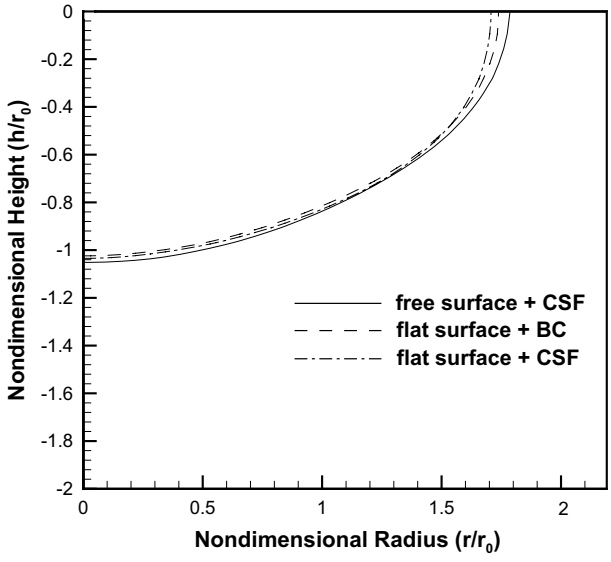

Fig. 7. Weld pool geometry for 20 ppm Fe–S with irradiation time of 5 s.

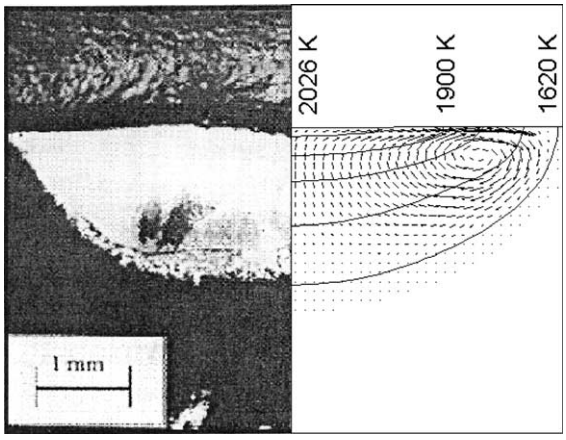

Fig. 8. Comparison of the predicted weld geometry to the experiment (Pitscheneder et al., 1996) for 20 ppm Fe–S at 5 s.

3.2. Weld pool calculation for gallium

Numerical calculation has been performed for the CO_2 laser welding experiment conducted by Limmaneevichitr and Kou (2000). Laser power has a Gaussian distribution and the target is gallium. The surface tension coefficient for gallium is assumed to be constant. The material properties and other information used by the simulation are given in Table 2. The 32×32, 37×37, and 52×52 grid systems are used for grid dependency test. Fig. 9 shows the weld pool geometry for gallium with irradiation time of 240 s with respect to grid size. The numerical mass losses of the target material during the calculation of free surface deformation for the 32×32, 37×37, and 52×52 grid systems are 0.0116%, 0.0173%, and 0.0310%, respectively. Fig. 10 shows the magnified free surface profile of the weld pool for gallium with irradiation time of 240 s with respect to grid size. The result from 37×37 grid system, showing converged weld pool shape and small mass error, is used for the following discussion. Fig. 11 shows

Table 2
Data used for calculation of velocity and temperature fields (Limmaneevichitr and Kou, 2000)

Property/parameter	Value
Density (kg/m^3)	6100.0
Surface tension at the melting temperature (N/m s)	0.718
Surface tension coefficient (N/m K)	-1×10^{-4}
Melting temperature (K)	302.9
Viscosity (kg/m s)	1.94×10^{-3}
Thermal conductivity of solid and liquid (J/m s K)	33.0
Specific heat of solid (J/kg K)	393.9
Specific heat of liquid (J/kg K)	409.7
Latent heat of melting (J/kg)	80×10^4
Beam radius (m)	2.95×10^{-3}
Laser power (W)	15
Target diameter (m)	25×10^{-3}
Target thickness (m)	10×10^{-3}

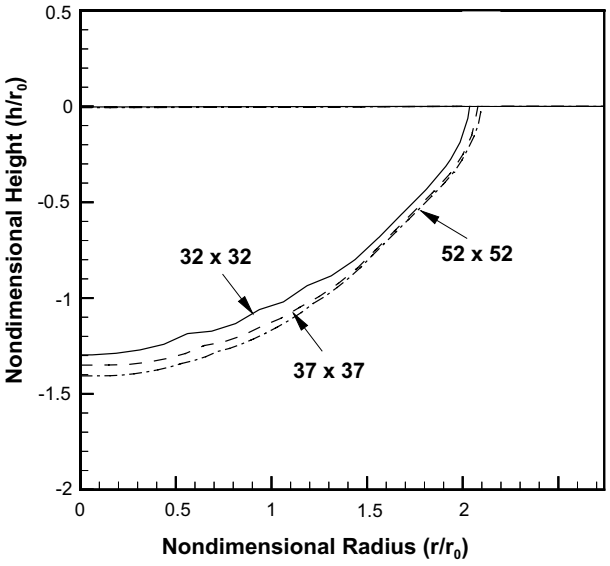

Fig. 9. Grid dependency of weld pool geometry for gallium with irradiation time of 240 s.

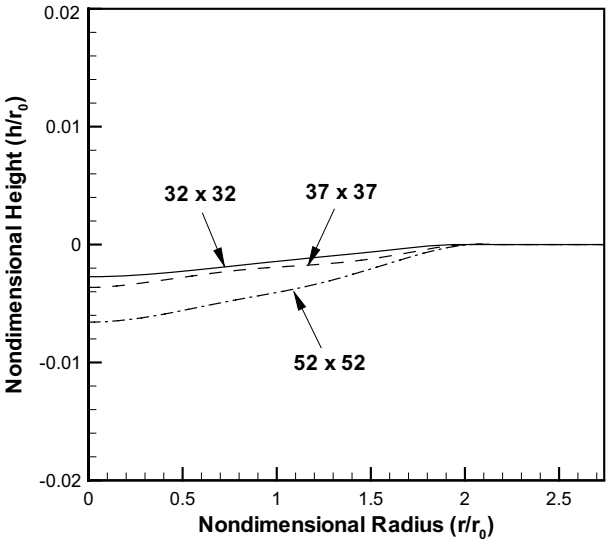

Fig. 10. Free surface profile of weld geometry for gallium with irradiation time of 240 s.

the comparison of the weld pool size with and without free surface effect. The aspect ratio of the weld pool is about 0.32 and the pool width and depth with free surface evolution are about 10% greater than those without free surface evolution. The *Pe* number of gallium weld pool is 20 and *We* number is 0.12. It is evident from the results of steel and gallium welding process that the aspect ratio of the weld pool becomes larger if *Pe* number decreases. The weld pool surface deformation becomes larger if *Pe* number increases, but it is negligible if *We* number is greater than 0.1. Fig. 12 depicts the comparison of the predicted weld geometry to that of

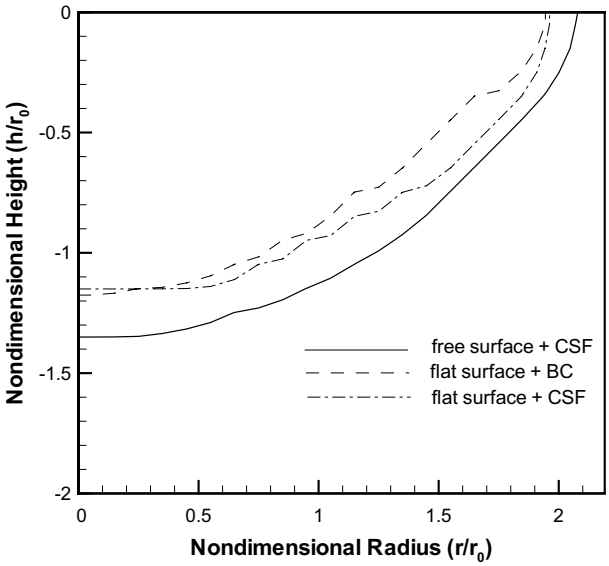

Fig. 11. Weld pool geometry for gallium with irradiation time of 5 s.

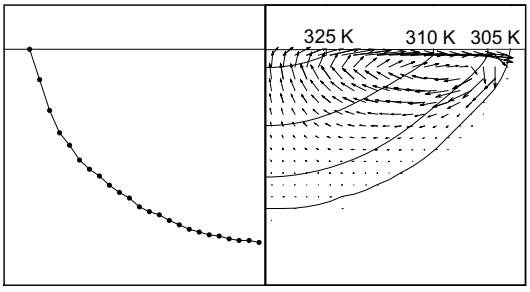

Fig. 12. Comparison of the predicted weld geometry to the experiment (Limmaneevichitr and Kou, 2000) for gallium with irradiation time of 240 s.

the experimental data. It is shown that the predicted weld pool width agrees well with that of experimental data, but the predicted weld pool depth is a little smaller.

3.3. Weld pool calculation for alumina (Al_2O_3)

In this case, numerical calculation has been performed for the CO_2 laser welding experiment conducted by Hirsch et al. (1998) Laser power distribution is top hat and radiative heat transfer is considered on the weld pool surface. The surface tension coefficient for alumina is assumed to be constant. The material properties and other information pertaining to the simulation are given in Table 3. The 35×25, 44×34, and 50×40 grid systems are used for grid dependency test. Fig. 13 shows the weld pool geometry for alumina at steady state with respect to grid size. The numerical mass losses of the target material during the calculation of free surface deformation for the 35×25, 44×34, and 50×40 grid systems are -0.0001%, -0.0008%, -0.0007%, respectively. Fig. 14 shows the magnified free surface profile of the alu-

Table 3
Data used for calculation of velocity and temperature fields (Hirsch et al., 1998)

Property/parameter	Value
Density (kg/m^3)	3000.0
Surface tension at the liquidus temperature (N/m s)	0.7
Surface tension coefficient (N/m K)	-6×10^{-5}
Liquidus temperature (K)	2327.0
Solidus temperature (K)	2101.0
Viscosity (kg/m s)	0.105
Thermal conductivity of solid (J/m s K)	5.44
Thermal conductivity of liquid (J/m s K)	4.8
Specific heat of solid (J/kg K)	1424.0
Specific heat of liquid (J/kg K)	1465.0
Latent heat of melting (J/kg)	1.05×10^{6}
Beam diameter (m)	2.2×10^{-3}
Laser power density(W/m^2)	64.0×10^{6}
Target diameter (m)	1.27×10^{-2}
Target thickness (m)	1.27×10^{-2}

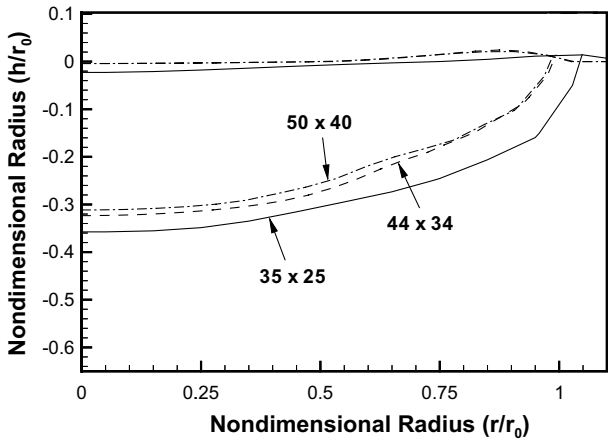

Fig. 13. Grid dependency of weld pool geometry for alumina at steady state.

mina weld pool at steady state with respect to grid size. It is noted that the free surface profiles are almost the same as those of the steel and gallium weld pool but the deformation of the weld pool surface is clearly shown in the welding process of alumina. For the following discussion, the result from 50×40 grid system, showing converged weld pool shape and small mass error, is used. Fig. 15 indicates that the comparison of the weld pool size with and without free surface effect. The width and depth of the weld pool with free surface evolution are about 2–4% greater than those without free surface evolution. The *Pe* number of alumina weld pool is 53 and *We* number is about 0.01. While the *Pe* number of alumina weld pool is smaller than that of steel, the aspect ratio of the alumina weld pool, about 0.17, is smaller than that of the steel weld pool because a small amount of heat, that could be transferred to the alumina substrate by conduction, is removed by radiation. It is evident that the weld pool surface deformation

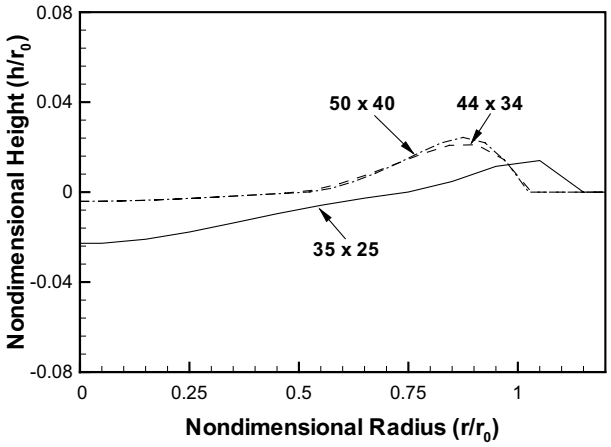

Fig. 14. Free surface profile of weld geometry for alumina at steady state.

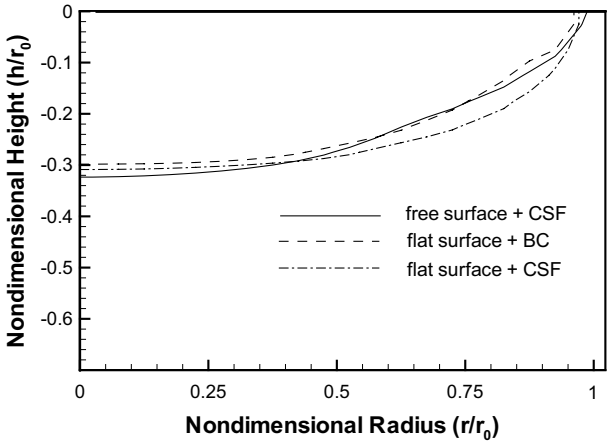

Fig. 15. Weld pool geometry for alumina at steady state.

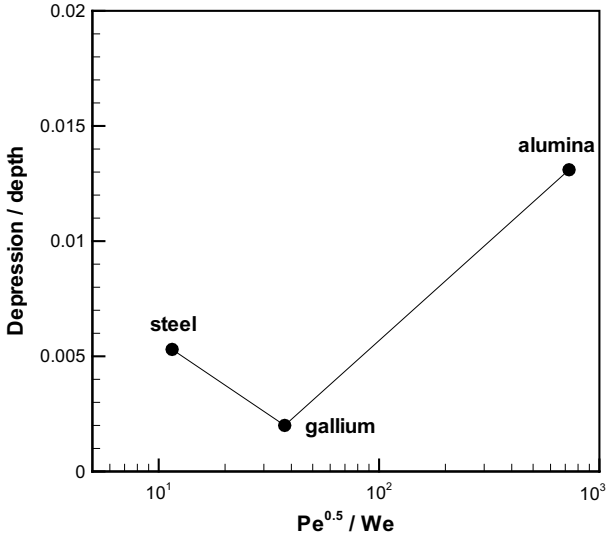

Fig. 16. Relation of weld pool surface deformation and dimensionless parameter of *Pe* number and *We* number.

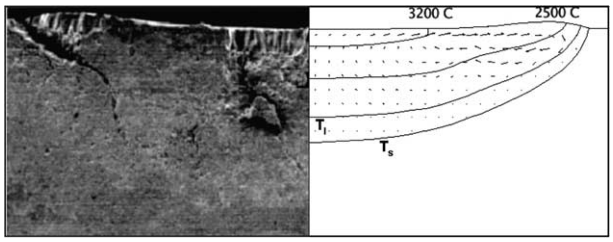

Fig. 17. Comparison of the predicted weld geometry to that of the experiment (Hirsch et al., 1998) for alumina at steady state.

is obvious if *Pe* number is larger and *We* number is much smaller than 1. In Fig. 16 the relation of the dimensionless depression (depression/depth of liquid pool) and dimensionless parameter, $\sqrt{Pe}/We$, is plotted. The dimensionless depression is about 0.0037 when $\sqrt{Pe}/We$ is the order of 10. But it increases up to 0.01 when $\sqrt{Pe}/We$ is about 700. Thus, the weld pool surface deformation should be considered when $\sqrt{Pe}/We$ is greater than the order of 10. Fig. 17 depicts the comparison of the predicted weld geometry to that of the experimental data. It is shown that the predicted weld pool shape agrees well with that of experiment and also the calculated weld pool depth and width are 0.43 mm and 2.15 mm, which is similar to 0.3 mm and 2.1 mm obtained from the experiment.

4. Conclusions

In this work, numerical analysis has been conducted on the dynamics of weld pool with surface deformation during low-energy density laser welding process. Modified CSF method is employed to incorporate Marangoni effect with deformable free surface in fixed grid system. The present numerical model reasonably simulates the data from the experiment. The free surface elevates near the weld pool edge and descends at the center of the weld pool if $d\sigma/dT$ is dominantly negative. The predicted width and depth of the weld pool with moving surface are a little greater than those with flat weld pool surface. It is believed that the oscillation of the weld pool surface during the melting process enhances the rate of convective heat transfer in the weld pool. In low-power density laser welding, the width of the weld pool is wider and the depth of the weld pool is shallower as the *Pe* number becomes larger. The present analysis with moving free surface should be considered when *Pe* number is larger and *We* number is much smaller than one since the deformation of the weld pool surface is noticeable as *Pe* number increases and *We* number decreases, especially when $\sqrt{Pe}/We$ is greater than order of 10.

Acknowledgment

This work was supported by Korea Research Foundation Grant (KRF-2002-041-D00071).

References

Basu, S., Debroy, T., 1992. Liquid metal expulsion during laser irradiation. J. Appl. Phys. 72, 3317–3322.
Bauerle, D., 1996. Laser Processing and Chemistry. Springer.
Brackbill, J.U., Kothe, D.B., 1996. Dynamical modeling of surface tension. LA-UR-96-1706.
Brackbill, J.U., Kothe, D.B., Zemach, C.A., 1992. Continuum method for modeling surface tension. J. Comput. Phys. 100, 335–354.
Chan, C., Mazumder, J., Chen, M.M., 1984. Two-dimensional transient model for convection in laser melted pool. Metall. Trans. A 15A, 2175–2184.
Duley, W.W., 1999. Laser Welding. John Wiley & Sons, Inc.
Hirsch, J.W., Olson, L.G., Nazir, Z., Alexander, D.R., 1998. Axisymmetric laser welding of ceramics: Comparison of experimental and finite element results. Opt. Lasers Eng. 29, 465–484.
Kim, W.S., Sim, B.C., 1997. Study of thermal behavior and fluid flow during laser surface heating of alloys. Numer. Heat Transfer A 31, 703–723.
Kothe, D.B., Mjolsness, R.C., 1991. RIPPLE: A new model for incompressible flows with free surfaces. AIAA 91-3548.
Limmaneevichitr, C., Kou, S., 2000. Experiments to simulate effect of Marangoni convection on weld pool shape. Weld. J. 79, 231s–237s.
Marathe, A.G., Ravi, M.R., 2004, Simulation of laser and electron beam melting problems. In: XVII National and VI ISHMT/ASME Heat and Mass Transfer Conference, IGCAR, Kalpakkam, January 5–7, HMT-2004-K7, pp. 57–62.
Pitscheneder, W., Debroy, T., Mundra, K., Ebner, R., 1996. Role of sulfur and processing variables on the temporal evolution of weld pool geometry during multikilowatt laser beam welding of steels. Weld. J. 75, 71s–80s.
Rider, W.J., Kothe, D.B., 1998. Reconstructing volume tracking. J. Comput. Phys. 141, 112–152.
Robert, A., Debroy, T., 2001. Geometry of laser spot welds from dimensionless numbers. Metall. Trans. B 32B, 941–947.
Sahoo, P., Debroy, T., McNallan, M.J., 1988. Surface tension of binary metal—surface active solute systems under conditions relevant to welding metallurgy. Metall. Trans. B 19B, 483–491.
Sasmal, G.P., Hochstein, J.I., 1994. Marangoni convection with a curved and deforming free surface in a cavity. J. Fluid Eng. 116, 577–582.
Swaminathan, C.R., Voller, V.R., 1993. On the enthalpy method. Int. J. Numer. Meth. Heat Fluid Flow 3, 233–244.